

Two-dimensional simulation of filaments in barrier discharges

Gunther Steinle^{†§}, Doerte Neundorf[†], Wolfgang Hiller[†] and Martin Pietralla[‡]

[†] Department FV/FLO, Robert Bosch GmbH, Postfach 106050, D-70049 Stuttgart, Germany

[‡] Department of Experimental Physics, University of Ulm, D-89069 Ulm, Germany

Received 8 January 1999, in final form 17 March 1999

Abstract. We present a fluid model for barrier discharges in air at atmospheric pressure with spectral resolved photonic secondary processes, implemented with general finite-element software. The results show five different discharge phases, a homogenous and a space-charge dominated avalanche phase, a phase of dielectric charging with field enhancement due to positive ions causing streamer formation, a cathode streamer and a subsequent glow-discharge phase with a cathode-fall region. Quenching of the microdischarge occurs after a few nanoseconds by the increasing charge on the dielectric. While the capacity of the dielectric has nearly no influence on the energetic efficiency of radical production and vacuum-UV-irradiation of the dielectric, a higher voltage causes a small decrease in radical efficiency and a significant increase in the efficiency of VUV-irradiation of the dielectric.

1. Introduction

In the following paper we present simulations of dielectric barrier discharges with a general finite-element software [1]. Dielectric barrier discharges (DBDs) occur when an electrical field exceeding the breakdown field is applied on two electrodes, at least one of them being covered with a dielectric layer. The developing discharge channels (filaments) are quenched by the growing surface charge on the dielectric. Since the quenching occurs within a few nanoseconds the heavy particles stay cold and thermal defects on the dielectric are avoided. DBDs are used for ozone synthesis in air [2]. Further possible applications are surface cleaning and etching [3], thin-film production [4] or surface modification of polymers (mainly crosslinking and polarization) [5]. Although the production of oxygen radicals in an air discharge is several orders of magnitude higher than the number of emitted VUV-photons ($\lambda < 175$ nm), the latter have penetration depths in polymers of several nanometres and their influence on adhesive properties is possibly not negligible [6, 7].

2. Modelling

2.1. Fluid equations

In order to calculate plasma volume and surface processes during a discharge in air at atmospheric pressure, a multidimensional description with one time and at least two spatial dimensions is necessary, otherwise the space-charge field cannot be calculated self-consistently [8, 9]. The space-charge field is calculated by solving simultaneously the

Poisson equation (1) and the differential equations (2)–(4) giving a one-moment description for particle transport. These equations define what is called a fluid or partial equilibrium description, because relaxation effects of the electron energy distribution are assumed to be negligible. Thus, transport and the production of charged particles can be assumed to be directly field dependent. A three-moment description [10] as well as Monte Carlo simulations [2, 11] have shown that a fluid description is appropriate for streamer discharges at atmospheric pressure, when photo-ionization is included as a non-local secondary effect. Runaway effects turn out to be negligible [11]. The one-moment continuity equations (2)–(4) for charged particles include inelastic processes, such as ionization by electrons (α), attachment of electrons to oxygen (η), recombination (β) of negatively and positively charged particles as well as photo-ionization (S_{ph}). For the field dependence of the effective ionization coefficient $\alpha_{eff} = \alpha - \eta$, we use an analytic approximation from Hartmann [12]. The field dependence of the attachment coefficient η can also be described by a simple expression [13]. Both expressions are valid for all relevant values of the reduced field E/N .

$$\Delta V = \frac{e}{\epsilon_r \epsilon_0} (N_e + N_n - N_p) \quad (1)$$

$$\nabla \cdot (\nu_e N_e - D \nabla N_e) - (\alpha - \eta) | \nu_e | N_e + \beta N_p N_e + \frac{\partial N_e}{\partial t} = S_{ph} \quad (2)$$

$$\nabla \cdot (\nu_p N_p) + \beta_n N_p N_n + \frac{\partial N_p}{\partial t} = S_{ph} + \alpha | \nu_e | N_e \quad (3)$$

$$\nabla \cdot (\nu_n N_n) + \beta_n N_p N_n + \frac{\partial N_p}{\partial t} = \eta | \nu_e | N_e. \quad (4)$$

§ Correspondence to: Siemens AG, Dept. ZT KM 4, D-81730 Munich.

Ion drift is about a hundred times smaller than electron drift, but the axial component is important during the glow discharge phase and thus included. The influence of the radial component on the current characteristics (rise time, peak value) is about 3–4% [14] and thus neglected. We use $\mu_i = 3.42 \times 10^{-4} \text{ m}^2 \text{ V}^{-1} \text{ s}^{-1}$ as mobility for positive and negative ions. The electron mobility μ_e and the constants for radial (D_r) and axial (D_l) diffusion are assumed to be independent of the electric field ($\mu_e = 3.82 \times 10^{-2} \text{ m}^2 \text{ V}^{-1} \text{ s}^{-1}$, $D_{11} = D_r = 0.22 \text{ m}^2 \text{ s}^{-1}$, $D_{22} = D_l = 0.18 \text{ m}^2 \text{ s}^{-1}$). The values refer to nitrogen [8] and are used as an approximation for air. The rise time and the maximum of the external current with the more complicated value for the electron drift in air given in [13] differ by less than 15% [14]. The externally influenced current is derived from Sato's equation [15]:

$$I_{ext} = \frac{1}{V_a} \iint \int_{Gap} \mathbf{E}_L \cdot \mathbf{j}_c \, dV. \quad (5)$$

Here \mathbf{E}_L is the Laplace field (field without space charges), \mathbf{j}_c is the convection current in the gap and V_a the applied voltage. Equation (5) is valid as long as the applied voltage does not change during the discharge.

2.2. Secondary processes

Important secondary processes during the discharge are photo-ionization of oxygen molecules and the photoeffect on the cathode. We also take into account Auger electrons by impact of positive ions on the cathode with an efficiency of $\gamma_i = 5 \times 10^{-3}$. So the flux density of secondary electrons out of the cathode is given by

$$\mathbf{j}_{sek}(\mathbf{x}, t) = \gamma_i \mathbf{j}_p(\mathbf{x}, t) + \mathbf{j}_{ph}(\mathbf{x}, t) \quad (6)$$

where \mathbf{j}_p is the flux density of positive ions ($\mathbf{j}_p = N_p \mathbf{v}_p$) and \mathbf{j}_{ph} the flux density of UV/VUV-photons with sufficient energy to release photo electrons.

$$\mathbf{j}_{ph}(\mathbf{x}, t) = \sum_i \int_0^t \iiint \int_{Gap} \frac{p_{qi}}{p + p_{qi}} \frac{1}{\tau_i} \exp\left(-\frac{t-t'}{\tau_i}\right) \times S_{ex,i}(\mathbf{x}', t') g(\mathbf{x}, \mathbf{x}') \exp[-\mu_i |\mathbf{x} - \mathbf{x}'|] d^3x' dt' \quad (7)$$

with $g(\mathbf{x}, \mathbf{x}') = \cos(\theta) (4\pi |\mathbf{x} - \mathbf{x}'|^2)^{-1}$ as the geometric factor of the cathode and $S_{ex,i}$, p_{qi} and τ_i as the excitation rate, quenching pressure and lifetime of the i th molecular level. Since the main visible and near-UV-radiation originates from the second positive system of nitrogen, it has been chosen for secondary effects in [16] and [17]. For metal work functions exceeding 3.5 eV only higher energetic photons will contribute. We have only considered the VUV-emitting Birge–Hopfield system of nitrogen with an approximate quenching pressure of 30 Torr [13]. We have estimated the collision dominated lifetime in atmospheric pressure with $\tau \approx 0.45 \text{ ns}$. The integral is evaluated for discrete points (r) on the cathode. The angular part ($d\varphi$) leads to an exact elliptical integral of second order for $r = 0$ or when absorption in the gas can be neglected; in all other cases the integral is calculated approximately with an estimated error of less than 22% [14]. For photo-ionization of oxygen molecules, S_{ph} is calculated similarly to the photocurrent (7) by summation of all Birge–Hopfield levels and a modified

factor $g(\mathbf{x}, \mathbf{x}') = \eta_i \mu_i (4\pi |\mathbf{x} - \mathbf{x}'|^2)^{-1}$ with η_i as the corresponding photo-ionization efficiency [13]. Instead of evaluating the complete integral we make the approximation that all gas-ionizing photons are produced in a sphere around the centre of mass of radiation with a radius equal to the characteristic radius of the discharge. The estimated error is less than 25% for gap spacings less than 0.5 mm [14] and thus smaller than the uncertainty of the quenching pressure values given in [7] and [18].

2.3. Numerical method

We use the general Galerkin finite-element software FlexPDE™ [1] which provides great flexibility in boundary geometry and the formulation of equations. Therefore, we are also able to simulate discharges in a more complicated geometry (e.g. point to plane) as well as in electrostatic discharge problems without an external circuit [14]. To avoid Gibbs errors and to enhance the accuracy for small values (which is important for secondary processes) we use a logarithmic transformation of all density variables.

2.4. Initial and boundary conditions

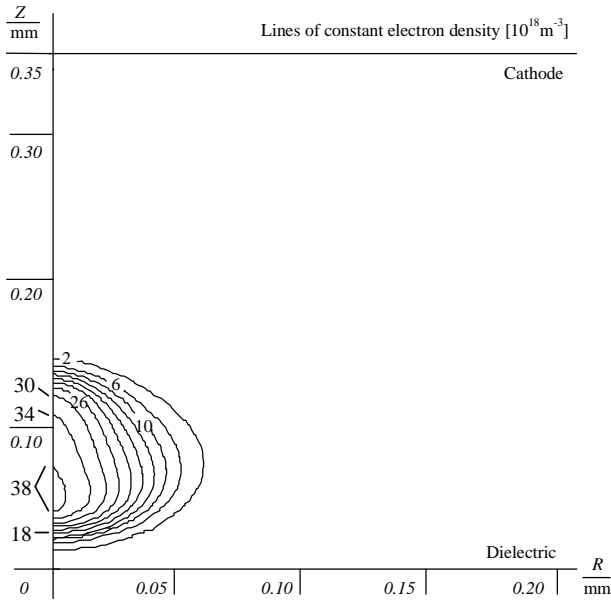
We choose a parallel-plate geometry with rotational symmetry. One electron is released from the cathode at $r = 0$ and it multiplies within the initially homogenous field. As long as the space charges do not influence the field the problem has a simple analytical solution, given by a Gaussian distribution:

$$N_e(\mathbf{x}, t) = \frac{1}{(4\pi t)^{3/2} D_r D_l^{1/2}} \times \exp\left\{-\frac{r^2}{r D_l t} - \frac{(z - v_{ez} t)^2}{4 D_l t} + (\alpha - \eta) |v_e| t\right\}. \quad (8)$$

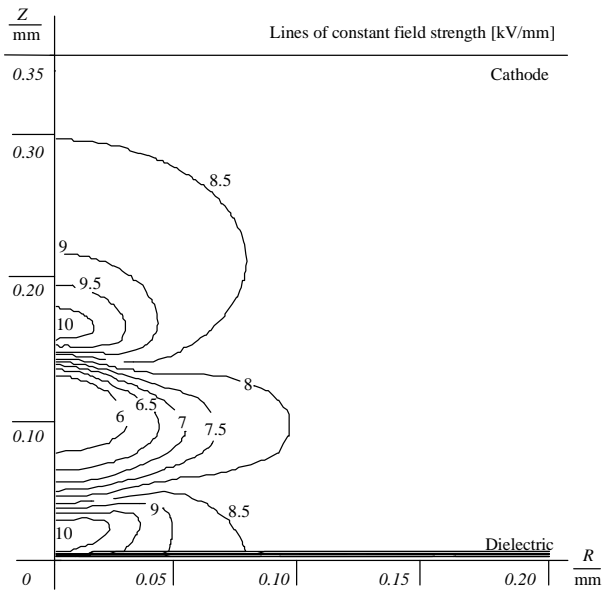
We start the simulation with the analytical solution for the undisturbed exponentially growing avalanche of some 100 electrons and an approximated ion distribution. During this phase the order of magnitude of photo-ionization is considered approximately by a homogenous background plasma of about 10^{10} m^{-3} , similar to as in [8, 19]. Because of the exponential avalanche the background plasma is soon determined only by the calculated photo-ionization S_{ph} and becomes inhomogeneous because of absorption in the gas.

We have used the following boundary conditions:

- (i) All radial derivations are set to zero on the axis and on the boundary $r = r_{\max}$.
- (ii) At the perfectly conducting cathode (equipotential surface) the electron density is j_{sek}/v_e , whereas the negative ion density is zero. For positive ions a boundary condition is necessary which takes into account the Auger neutralization on the cathode. This is similar to an 'absorbing' or 'open' boundary corresponding to a calculation in semi-infinite space. Since the partial differential equation (3) describing positive ions is of first order, the characteristics must have only one point in common with the given plane of the initial and boundary conditions. So the flux into the upper boundary can be calculated self-consistently from the values within the volume. In calculations with finite elements it is possible to have so-called 'natural' boundary conditions. Here a



(a)

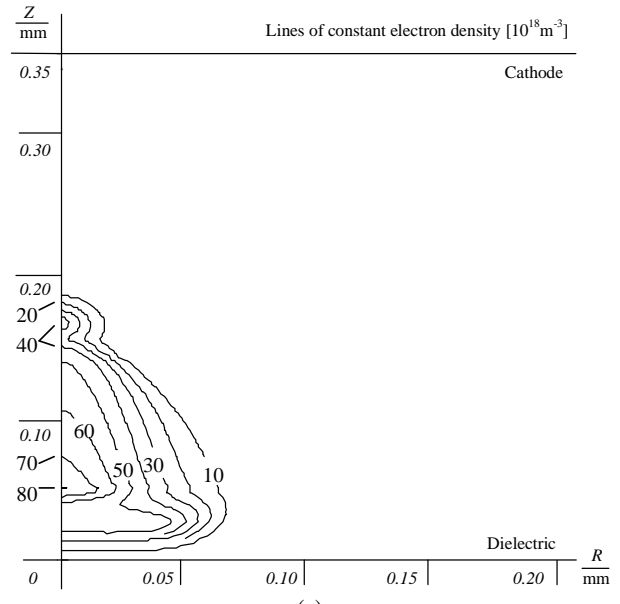


(b)

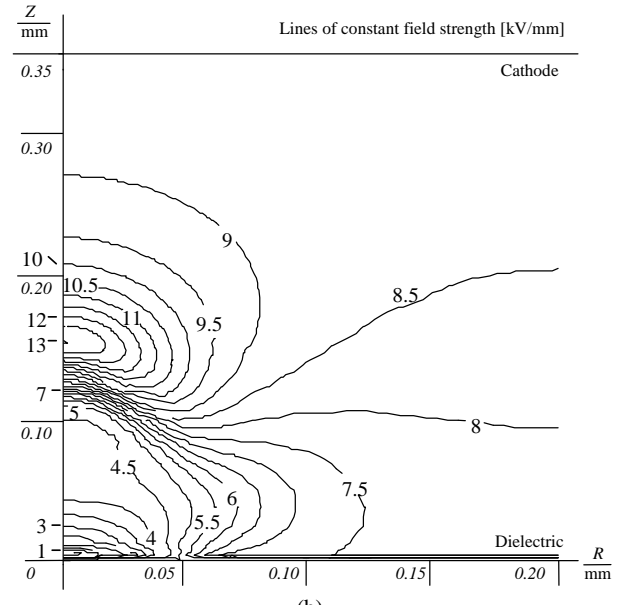
Figure 1. (a) Lines of constant electron density for $t_s = 0.54$ ns during the space-charge-dominated avalanche phase showing a shock-like axial profile due to nonlinear space-charge effects. Numbers shown in the plot correspond to the number density divided by 10^{18} m^{-3} . (b) The corresponding electric field given in units of kV mm^{-1} .

‘natural’ boundary condition gives the flux of particles normal to the boundary. Since we use a logarithmic transformation and divide each continuity equation by the respective density variable, our ‘natural’ boundary condition is equal to the drift velocity of positive ions at the boundary.

- (iii) The dielectric covers the anode and is assumed to adsorb all electrons and negative ions. So the current density is integrated over the time to obtain the charge density $\sigma(x, t)$ on the surface, which causes a jump in the axial displacement $\Delta D_z = \sigma$.



(a)

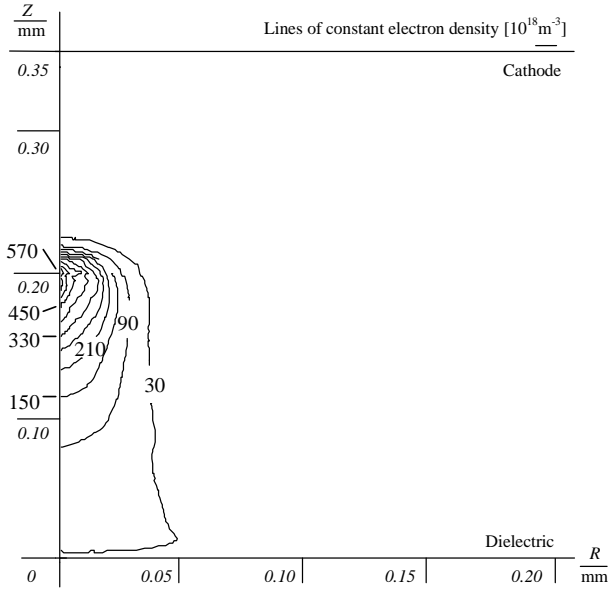


(b)

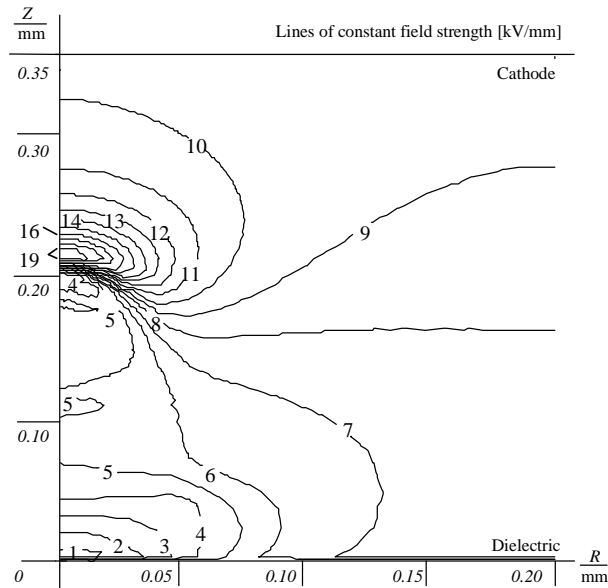
Figure 2. (a) The electron density for $t_s = 0.68$ ns after the electrons of the first avalanche are adsorbed on the dielectric. (b) The electric field in the gap is partly enhanced.

3. Dynamics of microdischarges

We choose a gap distance of $h = 0.35$ mm, a dielectric layer on the anode with $\epsilon_r = 3.3$ and a thickness $d = 0.35$ mm. The outer boundary is set to $r_{\text{max}} = 0.2$ mm. The applied DC voltage of 3800 V causes an initial electric field in the gap of 8.33 kV mm^{-1} . We can subdivide the development of a microdischarge filament into five different phases. During the first phase the distortion of the electrical field by space charges is negligible. The exact solution of the electron avalanche is given by a Gaussian distribution with characteristic radius $r_g = 2(D_i t)^{1/2}$. During this phase the simulation starts with an avalanche containing 684 electrons



(a)



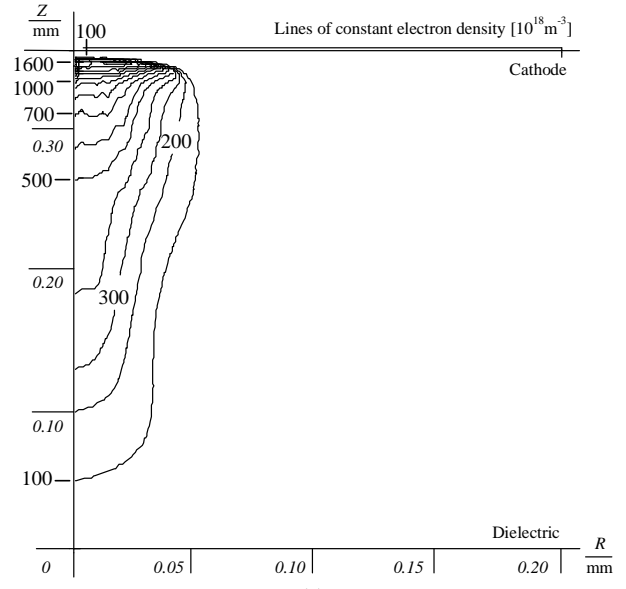
(b)

Figure 3. (a) The electron density for $t_s = 0.88$ ns during the cathode streamer phase growing to the cathode. (b) The electric field is shielded in the bulk by nearly 50%.

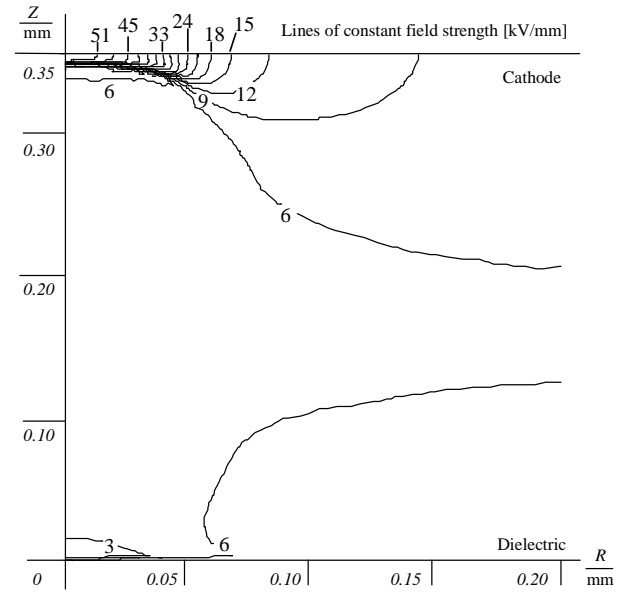
at $t = t_0 = 0.32$ ns after the first electron has been released from the cathode. This phase is not illustrated.

The following four phases are dominated by nonlinear space-charge effects. Figures 1–4 show the corresponding contours of electron density (a) and electric field (b).

(i) *Space-charge dominated avalanche phase* (simulation time $t_s = t - t_0 = 0.54$ ns). The plasma is beginning to shield the electric field in its bulk, thus increasing the value outside of it (figure 1(b)). This causes a plain region around the density peak of electrons followed by steeper axial gradients than the diffusion dominated undistorted Gauss distribution (figure 1(a)). The characteristic radial expansion ($1/e$ decay) of about $0.36 \mu\text{m}$ differs only slightly from the diffusion-dominated value of $r_g = 2(D_t t)^{1/2} = 0.28 \mu\text{m}$.



(a)



(b)

Figure 4. (a) The electron density for $t_s = 1.12$ ns after the arrival of the streamer at the cathode. (b) The electric field is strongly enhanced in the cathode-fall region.

(ii) *Charging of the dielectric* ($t_s = 0.68$ ns). During this phase the field in front of the dielectric is reduced by adsorbed electrons on the dielectric from the primary avalanche. This inhomogeneous charging causes a radial field reaching a peak value of about 4 kV mm^{-1} during the following streamer phase [14]. The corresponding radial drift of electrons determines the radial expansion of the charged area. The slow positive ions stay in the gap and cause a strong field enhancement with a peak value of 13 kV mm^{-1} at $z = 0.16$ mm in front of the surface (figure 2(b)). In the absence of secondary effects the field enhancement has no influence on the discharge, which stops immediately. Because of multiplication of the delayed electrons from secondary processes the field enhancement due to positive ions increases until the ionization rate overcompensates the

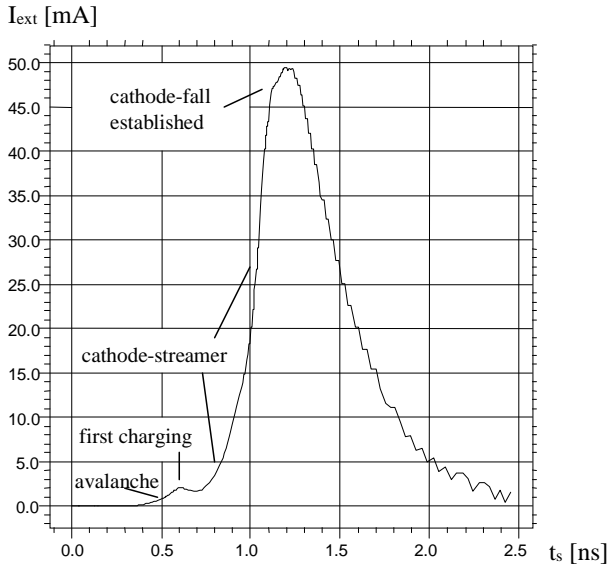


Figure 5. The different discharge phases can be distinguished in the current form influenced in the external circuit I_{ext} , the decay of the last phase (glow discharge) is slowed down by the slower charging rate of the dielectric at the end of the discharge.

electron loss due to drift and the streamer phase is initiated. At very high values of the applied field or large gaps this phase is omitted and a midgap streamer expanding in both directions (to the dielectric and cathode) is formed before the avalanche can reach the dielectric [14].

(iii) *Cathode streamer phase* ($t_s = 0.88$ ns). Now a nonlinear ionization potential wave forms a plasma channel, which grows from the dielectric to the cathode (cathode streamer). As pointed out by Wang and Kunhardt [9], the dynamics of a streamer is determined by the current continuity; the displacement current outside the plasma is transformed into the convection current inside. The value

of the electric field in the bulk is about $4\text{--}5$ kV mm⁻¹ (figure 3(b)).

(iv) *Glow discharge phase with cathode fall* ($t_s = 1.12$ ns). When the streamer reaches the cathode a glow discharge with a voltage drop (cathode fall) of roughly 300 V across about $6\text{--}8$ μm is established, which causes an approximate constant electric field with a value of about $40\text{--}50$ kV mm⁻¹ in front of the cathode (figure 4(b)). The peak value and the gradients of the electron density distribution reach their highest values. The electron density as well as the field enhancement of the cathode fall show a slow radial expansion during this phase, corresponding to an increase of the cathode-fall radius from about 30 μm to 50 μm until the end of the discharge at $t_s = 2.45$ ns. All peak values stay approximately constant during this phase, so it can be called a ‘quasi-stationary glow discharge’.

All these stages can be distinguished by the development of the external current I_{ext} (figure 5). The rise time (10–90%) is mainly determined by the streamer phase. As soon as the streamer reaches the cathode and the cathode fall region is established, the current shows a kink from overexponential rise to a nearly linear phase. The decay begins as soon as the decrease of drift velocities due to charging of the dielectric overcompensates the production rates. To the end of the discharge our calculated currents show a decreasing decay rate due to a reduced charging rate in agreement with simulations shown in [20] and measurements reported in [21].

4. The influence of barrier capacity and applied voltage

To investigate the influence of barrier capacity on the discharge we take the same electric field for the gap ($E_L = 8.33$ kV mm⁻¹, $h = 0.35$ mm) and vary the dielectric constant ϵ_r (1.53, 2.31, 3.3 and 4.62). The results are shown in

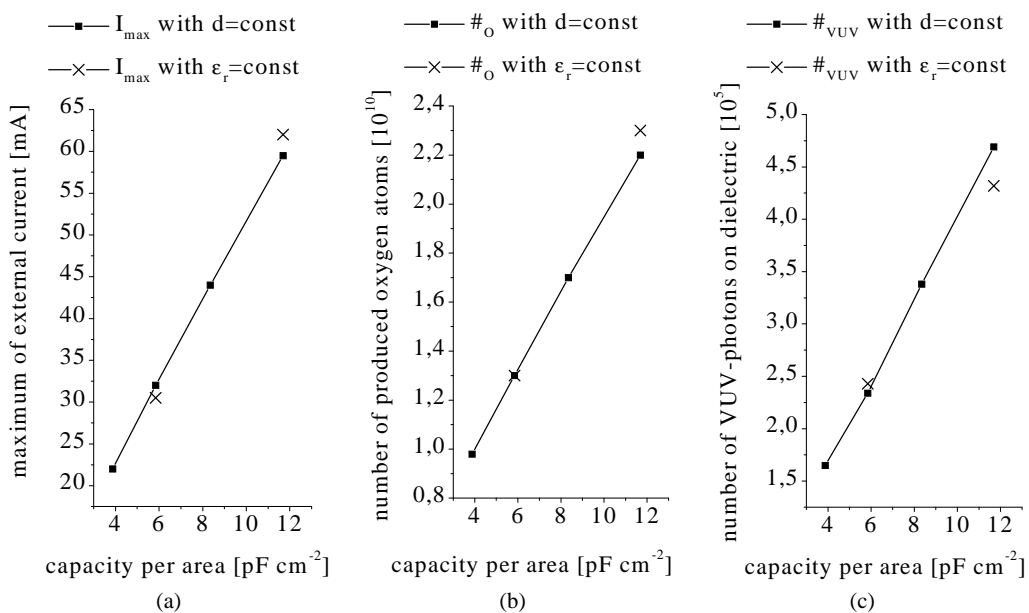


Figure 6. The maximum of the external current I_{ext} (a), the number of produced oxygen radicals (b) and VUV-photons reaching the dielectric (c) scale with barrier capacity (with constant Laplace field in the gap and constant gap width).

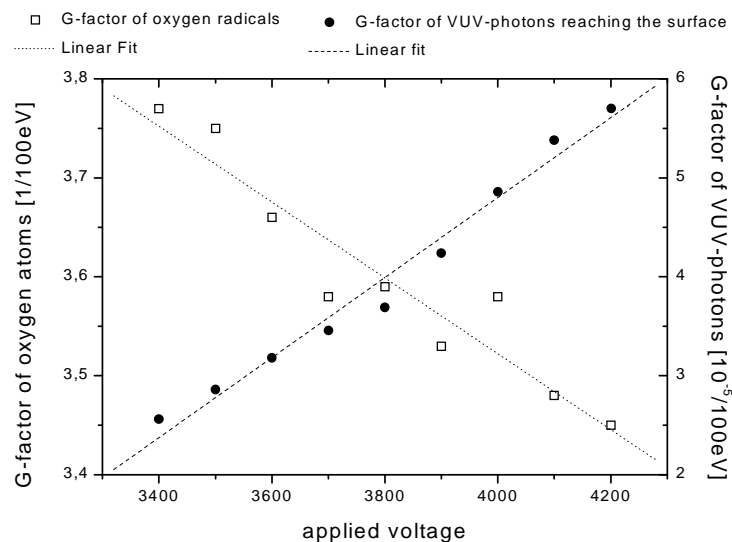


Figure 7. The influence of the applied voltage on the G -factors for oxygen radicals and VUV-photons (the number of oxygen atoms, respectively VUV-photons, on the dielectric per 100 eV input energy).

figures 6(a)–(c) (squares). In order to investigate the symmetry in ϵ_r/d we also change the thickness d (0.25 mm, 0.35 mm, 0.5 mm) with a constant value of the dielectric constant $\epsilon_r = 3.3$. These results are shown by crosses. For the investigated capacities the deviation from the symmetry is small.

The dynamics of the discharge is not seriously altered by changing the barrier capacity. With constant gap width and Laplace field in the gap the increase of the half-width of the external current I_{ext} turns out to be only about 16% from the smallest to the largest value of ϵ_r , while a change in rise times cannot be resolved [14]. The peaks of I_{ext} scale with the capacity (figure 6(a)). We calculated the production of oxygen atoms $\text{O}(^3\text{P})$ and $\text{O}(^1\text{D})$ by electron impact with the rate coefficient given in [19]. Dissociation of oxygen by excited nitrogen molecules is neglected. We also found a linear increase of radical production with an increase of capacity (figure 6(b)). The G -factor (number of oxygen atoms per 100 eV of input energy) is constant for all capacities with $G = 3.5(1)$. Additionally we calculated the VUV-radiation of the dielectric by nitrogen molecules emitting in the Birge–Hopfield band (12–14 eV). Figure 6(c) shows the number of VUV-photons reaching the dielectric. The corresponding energetic efficiency is about $G = 6.7(8) \times 10^{-5}$ VUV-photons reaching the dielectric per 100 eV energy input.

Figure 7 shows the variation of the G -factors with the applied voltage. While the production of oxygen radicals remains nearly constant (with decreasing tendency), the VUV-efficiency (G -factor of VUV-photons) increases with applied voltage.

5. Summary

The simulations show five different phases of a microdischarge in air. The main contributions for external current and particle production are from the two last stages, the cathode streamer phase and the subsequent glow discharge phase

with cathode fall. Quenching of the quasi-stationary glow discharge occurs due to a vanishing voltage drop along the gap because of the charging of the dielectric. The particle production (electrons, photons and oxygen atoms) is proportional to the barrier capacity, whereas the influence of the capacity on the dynamics of the discharge is negligible small, as long as the gap length and Laplace field in the gap stay the same. The energetic efficiency of oxygen production by electron impact dissociation and of vacuum-UV-irradiation of the barrier are not much influenced by the barrier capacity. While the onset voltage shows significant influence on the VUV-efficiency, the radical efficiency is not much altered. The number of high-energy photons (12–14 eV) is about five orders of magnitude smaller than the number of oxygen radicals produced.

References

- [1] FlexPDE™, Finite element Software, PDESolutions Inc., Web page: <http://www.pdesolutions.com>
- [2] Braun D, K uchler U and Pietsch G 1991 Microdischarges in air-fed ozonizers *J. Phys. D: Appl. Phys.* **24** 564–72
- [3] Falkenstein Z and Coogan J J 1997 Photoresist etching with dielectric barrier discharges in oxygen *J. Appl. Phys.* **82** 6273–80
- [4] Reitz U, Salge J G and Schwarz R 1993 Pulsed barrier discharges thin film production at atmospheric pressure *Surface Coatings Technol.* **59** 144–7
- [5] Greenwood O D, Boyd R D, Hopkins J and Badyal J P S 1996 *Polymer Surface Modification: Relevance to Adhesion* ed K L Mittal (Utrecht: VSP) pp 17–32
- [6] Hudis M 1972 Surface crosslinking of polyethylen using a hydrogen glow discharge *J. Appl. Polymer Sci.* **16** 2397–415
- [7] Liston E M, Martinu L and Wertheimer M R 1994 *Plasma Surface Modification of Polymers* ed M Strobel, C S Lyons and K L Mittal (Utrecht: VSP) pp 3–29
- [8] Dhali S K and Williams P F 1987 Two-dimensional studies of streamers in gases *J. Appl. Phys.* **62** 4696–707
- [9] Wang M C and Kunhardt E E 1990 Streamer dynamics *Phys. Rev. A* **42** 2366–73
- [10] Guo J M and Wu C H J 1993 Two dimensional nonequilibrium fluid models of streamers *IEEE Trans. Plasma Sci.* **21** 684–95

- [11] Kunhardt E E and Tzeng Y 1988 Development of an electron avalanche and its transition into streamers *Phys. Rev. A* **38** 1410–21
- [12] Hartmann G 1984 Theoretical evaluation of Peek's law *IEEE Trans. Industry Appl.* **20** 1647–51
- [13] Galimberti I and Badaloni S 1972 *Basic Data of Air Discharges* (Padova: University of Padova Press)
- [14] Steinle G 1998 Modellierung der Koronaentladung zur physikalischen Vorbehandlung von Polymeroberflächen *Diploma Thesis* Department of Experimental Physics, University Ulm
- [15] Sato N 1980 Discharge current induced by the motion of charged particles *J. Phys. D: Appl. Phys.* **13** L3–6
- [16] Kennedy J T 1995 Study of the avalanche to streamer transition in insulating gases *PhD Thesis* TU Eindhoven
- [17] Wu C and Kunhardt E E 1988 Formation and propagation of streamers in N_2 and N_2 - SF_6 mixtures *Phys. Rev. A* **37** 4396–406
- [18] Teich T H and Bräunlich R 1985 UV and other radiations from discharges in artificial air and its constituents *Proc. VIII Int. Conf. on Gas Discharges and Applications* vol 1 (Oxford: Pergamon, Leeds University Press) pp 441–4
- [19] Li J and Dhali S K 1997 Simulation of microdischarges in a dielectric-barrier discharge *J. Appl. Phys.* **82** 4205–10
- [20] Braun D, Gibalov V and Pietsch G 1992 Two-dimensional modelling of the dielectric barrier discharge in air *Plasma Sources Sci. Technol.* **1** 166–74
- [21] Brosche Th 1998 Erweitertes Teilentladungsmeßverfahren durch Erfassung neuer Impulsparameter *PhD Thesis* TU Darmstadt (Aachen: Shaker)